Atmospheric Environment 138 (2016) 191–204

Contents lists available at ScienceDirect

Atmospheric Environment

journal homepage: www.elsevier.com/locate/atmosenv

Influence of the vertical absorption profile of mixed Asian dust plumes on aerosol direct radiative forcing over East Asia

Young Min Noh [a], Kwonho Lee [b], Kwanchul Kim [a], Sung-Kyun Shin [c], Detlef Müller [d, *], Dong Ho Shin [e]

[a] International Environmental Research Center, Gwangju Institute of Science & Technology (GIST), Republic of Korea
[b] Department of Atmospheric and Environmental Sciences, Gangneung-Wonju National University, Republic of Korea
[c] Research Institute for Radiation-Satellite, Gangneung-Wonju National University, Republic of Korea
[d] School of Physics, Astronomy and Mathematics, University of Hertfordshire, Hertfordshire, UK
[e] Air Quality Forecasting Centre, Climate and Air Quality Research Department, National Institute of Environmental Research, Republic of Korea

HIGHLIGHTS

- Aerosol direct radiative forcing (ADRF) and heating rate profiles were estimated.
- Vertical profiles of extinction coefficient and SSA are shown.
- The ADRF is affected by the vertical distribution and absorption of aerosols.
- Large errors of the radiative effect can be induced by applying a layer-mean SSA.

ARTICLE INFO

Article history:
Received 7 March 2016
Received in revised form
26 April 2016
Accepted 27 April 2016
Available online 8 May 2016

Keywords:
aerosol direct radiative forcing
Heating rate
Single-scattering albedo
Dust
Pollution

ABSTRACT

We estimate the aerosol direct radiative forcing (ADRF) and heating rate profiles of mixed East Asian dust plumes in the solar wavelength region ranging from 0.25 to 4.0 μm using the Santa Barbara Discrete Ordinate Atmospheric Radiative Transfer (SBDART) code. Vertical profiles of aerosol extinction coefficients and single-scattering albedos (SSA) were derived from measurements with a multi-wavelength Raman lidar system. The data are used as input parameters for our radiative transfer calculations. We considered four cases of radiative forcing in SBDART: 1. dust, 2. pollution, 3. mixed dust plume and the use of vertical profiles of SSA, and 4. mixed dust plumes and the use of column-averaged values of SSA. In our sensitivity study we examined the influence of SSA and aerosol layer height on our results. The ADRF at the surface and in the atmosphere shows a small dependence on the specific shape of the aerosol extinction vertical profile and its light-absorption property for all four cases. In contrast, at the top of the atmosphere (TOA), the ADRF is largely affected by the vertical distribution of the aerosols extinction. This effect increases if the light-absorption capacity (decrease of SSA) of the aerosols increases. We find different radiative effects in situations in which two layers of aerosols had different light-absorption properties. The largest difference was observed at the TOA for an absorbing aerosol layer at high altitude in which we considered in one case the vertical profile of SSA and in another case the column-averaged SSA only. The ADRF at the TOA increases when the light-absorbing aerosol layer is located above 3 km altitude. The differences between height-resolved SSA, which can be obtained from lidar data, and total layer-mean SSA indicates that the use of a layer-mean SSA can be rather misleading as it can induce a large error in the calculation of the ADRF at the TOA, which in turn may cause errors in the vertical profiles of heating rates.

1. Introduction

The uncertainty in estimating the aerosol radiative effect is one of the major uncertainties in predicting climate change. The radiative forcing calculated by the difference in net radiative flux density between an aerosol-laden and an aerosol-free atmosphere at the surface, at the top of the atmosphere (TOA), and within the atmosphere column can be changed by the aerosols in the atmosphere. These effects are strongly dependent on the optical properties of the aerosol. The direct effect of non-absorbing aerosols –

* Corresponding author.
E-mail address: d.mueller@herts.ac.uk (D. Müller).

http://dx.doi.org/10.1016/j.atmosenv.2016.04.044

such as sulphates – produces an overall cooling of the atmosphere, while partly absorbing aerosols – such as black and organic carbon – can lead to either a cooling or a warming, depending on the aerosols' properties and underlying albedo. Number, size distribution, shape, composition, and morphology of atmospheric aerosol have a high variability in time and space. Another important parameter for radiative forcing calculation is the vertical distribution of the aerosol particles (Meloni et al., 2005; Zarzycki and Bond, 2010; Samset and Myhre, 2011).

A variety of modeling (Schulz et al., 2006; Myhre et al., 2013; Vuolo et al., 2014) and measurements studies (Bellouin et al., 2008; Quaas et al., 2008; Remer and Kaufman, 2006; Noh et al., 2012; Mishra et al., 2014; Feng et al., 2016) to assess and reduce the uncertainty of aerosol direct radiative forcing (ADRF) have been conducted. The Aerosol Robotic Network (AERONET) provides long-term column integrated aerosol optical depth (AOD) of globally distributed sites (Dubovik et al., 2002; Eck et al., 2003, 2005; Giles et al., 2012). Advanced satellite measurements, such as the Moderate Resolution Imaging Spectroradiometer (MODIS) and the Multiangle Imaging Spectroradiometer (MISR), also offer almost globally distributed aerosol optical depth (Levy et al., 2007; Remer et al., 2008; Papadimas et al., 2009). These globally distributed AODs provided by AERONET and satellite data were used for input to aerosol radiative forcing calculations. However, those studies could not find consistent aerosol effects on climate change. This is mainly due to the large spatial and temporal variation of the aerosol concentration, mass and chemical composition as well as their relatively short lifetime in the atmosphere (Sundström et al., 2015). Another reason is the vertical distribution of atmospheric aerosols.

There is plenty of research work that suggests that the vertical distribution of aerosols is important information for an accurate estimation of the radiative and climatic effects of aerosols (Redemann et al., 2000; Highwood, 2003; Gadhavi and Jayaraman, 2006; Johnson et al., 2008; Noh et al., 2012; Mishra et al., 2015). Lidar networks in different areas on the globe provide information on the vertical distribution of aerosols on a continental scale (Welton et al., 2001; Sugimoto and Uno, 2009; Pappalardo et al., 2014). The European Aerosol Research Lidar Network (EARLINET) was founded in 2000 as a research project for establishing a quantitative, comprehensive, and statistically significant database for the horizontal, vertical, and temporal distribution of aerosols in Europe (Pappalardo et al., 2014). Automated two-backscatter (532 and 1064 nm) and one-polarization (532 nm) lidars are operating at 20 locations around the Asian continent with the goal of observing Asian dust and aerosol pollution from anthropogenic sources (Sugimoto and Uno, 2009). Space-borne lidars such as the Cloud-Aerosol Lidar and Infrared Pathfinder Satellite Observation (CALIPSO) launched in 2006 (Winker et al., 2003), provide vertical profiles of aerosol and cloud extinction with global coverage (Huang et al., 2009; Winker et al., 2009, 2010).

Guan et al. (2010) found that vertical absorption profiles drastically influence the profiles of forcing and heating rates. Noh et al. (2012) reported that highly absorbing particles within Asian dust layers may play a significant role in the increase of the radiative forcing and heating rates. However, the correct assessment of the impact of the vertical-distributed aerosol absorption characteristics on radiative forcing, commonly expressed in terms of the aerosol single-scattering albedo (SSA), remains a challenge as vertical profiles of light-absorption cannot be measured directly (Arnott et al., 2006).

Microphysical retrieval algorithms, i.e. inversion with regularization that use as input backscatter coefficients measured at three wavelengths and extinction coefficients measured at two wavelengths (Müller et al., 1999a; Veselovskii et al., 2002) are the most practicable method to retrieve vertically resolved SSA of aerosol pollution. Successful applications of the method of inversion with regularization can be found in, e.g., Murayama et al. (2004), Veselovskii et al. (2002), Müller et al. (2003; 2005), Tesche et al. (2008), and Noh et al. (2009, 2011). However, radiative forcing studies that use vertically resolved SSA retrieved with data inversion have not been carried out yet.

Mineral dust also has considerable influence on the Earth's radiation budget (Meloni et al., 2005). This mineral dust shows different optical and light absorption properties compared to anthropogenic and smoke particles (Dubovik et al., 2002; Russell et al., 2010). Since the anthropogenic emissions in Asia are projected to further increase in future (Ohara et al., 2007), the possibility that Asian dust plumes can be mixed with other, man-made pollution containing black carbon and/or smoke particles also will increase. Shin et al. (2015) demonstrates this mixing of dust with man-made pollution through identifying the pathway and the vertical position of dust-laden air masses over China during long-range transport using five years of multi-wavelength Raman lidar observations. This mixture of dust and anthropogenic particles causes changes in the optical properties of dust plumes (Noh, 2014). Shimizu et al. (2004), Tesche et al. (2009, 2011), and Noh et al. (2012) successfully separated mineral dust from the contribution of pollution particles in mixed-dust layers by using the linear particle depolarization ratio measured by lidar. However, studies related to the change of radiative effects caused by the mixing of dust and pollution particles based on observational data have not been performed until now.

Noh (2014) presents vertically-resolved and total layer-mean optical and microphysical parameters including SSA of mixed dust plumes and demonstrates that the addition of pollution particles increases the light-absorption property of mixed-dust plumes. In this study, for the first time, we estimate the direct shortwave aerosol radiative forcing and heating rate profiles of mixed-dust plumes using aerosol optical properties (extinction and SSA) obtained by Noh (2014) as input parameters for radiative transfer calculations. This sensitivity study also considers the sensitivity of radiative forcing with respect to SSA and aerosol layer height.

Section 2 describes the methodology to retrieve the vertically-resolved optical data and the radiative forcing calculation. Section 3 presents the results of calculated radiative forcing by measured and simulated data. Section 4 contains a summary and conclusion.

2. Methodology

2.1. Vertically-resolved optical data

East Asian dust plumes mixed with man-made pollution were observed with multi-wavelength Raman lidar at Gwangju (35.10°N, 126.53°E), South Korea. The system provides vertical profiles of particle backscatter coefficients at 355, 532, and 1064 nm, and extinction coefficients at 355 and 532 nm. The optical data serve as input for an inversion algorithm that provides profiles of microphysical particle properties which subsequently are used for computing single-scattering albedo. This study presents results of mixed dust plumes observed on 24 February 2004, 9 and 18 March 2004, 2 April 2004, and 24 February and 4 May 2005. The optical data of the mixed dust plumes were separated into the pure dust content and the contribution by anthropogenic pollution, i.e. the non-dust part. The linear particle depolarization ratio measured at 532 nm was used for this separation (Shimizu et al., 2004; Noh et al., 2012; Noh, 2014). The backscatter and extinction coefficients then were used to derive single-scattering albedo of the anthropogenic-pollution part of the mixed-dust plumes (Müller et al., 1999a, 1999b; 2000). This was done by retrieving

microphysical parameters with the inversion algorithm and subsequently using these parameters in Mie-scattering calculations for the computation of SSA.

We used the value 0.96 ± 0.02 at 532 nm for the SSA of pure dust. This value was obtained from SSA of dust observed in various dust source regions. In another step the "total (dust + pollution)" SSA of these mixed-dust plumes was calculated by using the optical depth of the dust and the pollution as weighting function. Details on the measurements, retrieval of SSA, and analysis are found in the publication by Noh (2014).

Vertically-resolved extinction coefficients and single-scattering albedos at 355, 532, and 1064 nm for dust and anthropogenic-pollution particles, and the total amount of aerosol particles (dust + pollution), respectively, are used as input parameters for computations with the radiative transfer model. The profiles of extinction and single-scattering albedo used in this study are obtained directly from results presented by Noh (2014).

In the case of SSA we obtain its value at 532 nm from the inversion algorithm. The SSAs at 355 and 1064 nm were retrieved by using the wavelength-dependence of pollution particles from 440 to 1020 nm by AERONET sun/sky radiometer data. Negative wavelength dependence, i.e. $dSSA/d\lambda < 0$, has been found for pollution particles observed by AERONET sun/sky radiometer in Mexico City and the Maldives (Dubovik et al., 2002; Russell et al., 2010). In the case of fine-mode-dominated aerosol particles, i.e. high Ångström exponents, SSA decreases with increasing observation wavelength. This effect is in part caused by the relatively weak wavelength dependence of the imaginary part of the complex refractive index of black carbon (Bergstrom et al., 2007; Eck et al., 2003, 2005; 2010). Black carbon is the main absorbing component in fine-mode particles. This wavelength dependence of SSA of fine-mode pollution particles was also observed by Noh et al. (2012). Based on these previous research results we obtained the SSAs at 355 and 1064 nm.

In contrast to anthropogenic pollution particles, dust particles show positive slopes of the wavelength-dependent SSA, i.e. $dSSA/d\lambda > 0$ (Dubovik et al., 2002; Russell et al., 2010; Noh et al., 2012). The value of SSA of dust particles is assumed as 0.96 at 532 nm in this contribution. We use the average wavelength-dependence of pure dust for SSA in our research work. We obtained this wavelength-dependence from previous studies (Dubovik et al., 2002; Eck et al., 2005, 2010; Russell et al., 2010). The values of 0.91 and 0.98 at 355 and 1064 nm, respectively were applied in this research.

The total SSA ($SSA_{\mathbf{T}}$) of the mixed-dust plume for each aerosol layer was calculated using the weight factor (F) that determines the contribution of optical depth of dust and the anthropogenic pollution to the total optical depth of the mixed-dust plume. F was obtained from the aerosol optical depth (τ) of each individual aerosol layer as follows:

$$F_{D,n} = \frac{\tau_{D,n}}{\tau_{D,n} + \tau_{P,n}} \quad (1)$$

$$F_{P,n} = \frac{\tau_{P,n}}{\tau_{D,n} + \tau_{P,n}} \quad (2)$$

The subscript n denotes the individual particle layers, and τ_D and τ_P denote the particle optical depth of dust and the anthropogenic-pollution part in each of these layers, respectively.

The $SSA_{\mathbf{T}}$ of the individual layers was calculated from multiplying the SSA of dust ($SSA_{\mathbf{D}}$) by FD, and the SSA of the anthropogenic-pollution part ($SSA_{\mathbf{P}}$) by FP, and subsequently adding these two terms:

$$SSA_T = F_{D,n}SSA_{D,n} + F_{P,n}SSA_{P,n} \quad (3)$$

The column-integrated SSA ($SSA_{\mathbf{int}}$) for the height range from surface to 6-km altitude was calculated by adding the $SSA_{\mathbf{T}}$ of each layer, weighted by the ratio of aerosol optical depth, i.e.

$$SSA_{int} = SSA_{T1}\frac{\tau_1}{\tau_t} + SSA_{T2}\frac{\tau_2}{\tau_t} + \cdots + SSA_{Tn}\frac{\tau_n}{\tau_t} \quad (4)$$

The term τ_t is the column-integrated particle optical depth.

Fig. 1 shows the vertically-resolved extinction coefficient and SSA at 532 nm of dust, anthropogenic pollution, and total (dust + anthropogenic pollution) aerosol particles. These parameters were used as input for our radiative forcing calculations. Aerosols are detected only below 6 km height. Above 6-km height we used the assumption of aerosol-free air in our radiative forcing calculations. The $SSA_{\mathbf{int}}$ of the total aerosol is also shown in Fig. 1. Multiple aerosol layers were found on 24 February and 2 April 2004, and also on 24 February and 4 May 2005. A pure Asian dust layer (Fig. 1 (a)), respectively layers dominated by dust (Fig. 1 (d and f)) were observed above the planetary boundary layer (PBL).

2.2. Radiative forcing calculation

Aerosol direct radiative forcing (ADRF) in the shortwave region from 0.25 to 4.0 μm was calculated with the Santa Barbara Discrete Ordinate Atmospheric Radiative Transfer (SBDART) code. SBDART is based on the discrete ordinate approach. It has been developed by the University of California, Santa Barbara, for the analysis of a wide variety of radiative transfer problems encountered in satellite remote sensing and atmospheric energy budget studies (Ricchiazzi et al., 1998). SBDART assumes a plane parallel, vertically inhomogeneous atmosphere. This model computes the radiative transfer on the basis of a plane-parallel atmosphere under clear as well as cloudy sky conditions within the Earth's atmosphere and at the surface. In the present study, the computations have been done only for clear sky conditions assuming the US62 standard atmosphere (Sissenwine et al., 1962). We selected a vegetated land surface in the model, because our observation site is for the most part surrounded by mountains and farmland.

Most previous ADRF research work considered an exponential drop of aerosol extinction with height above ground. Different scale heights according to AOD were used. However, this is not a reasonable assumption for multi-aerosol layers as shown in Fig. 1. In such cases, the aerosol forcing calculation must take into account the vertical distribution of aerosol extinction and absorption. The aerosol radiative forcing at the TOA or at the surface may be similar with a comparable optical thickness, because the ADRF is strongly dependent on the aerosol amount (particle concentration). However, variable aerosol extinction profiles with height-dependent absorption coefficients strongly influence the forcing and heating rates, respectively (Meloni et al., 2005; Guan et al., 2010). We used in our radiative forcing calculations the information on the vertical distribution of particles in terms of vertical profiles of the extinction measured with our lidar. Previous studies considered the aerosol extinction profiles (Won et al., 2004; Meloni et al., 2005; Guan et al., 2010; Noh et al., 2012). However, radiative forcing calculations that also used profiles of aerosol absorption were not yet performed. The aerosol absorption properties were expressed by SSA which was used as input parameter for the calculations with the radiative transfer model (RTM). Fig. 1 shows the extinction coefficients and single-scattering albedos of dust, anthropogenic pollution, and total (dust + pollution) particles that were used as input.

Since the multi-wavelength Raman lidar observations are

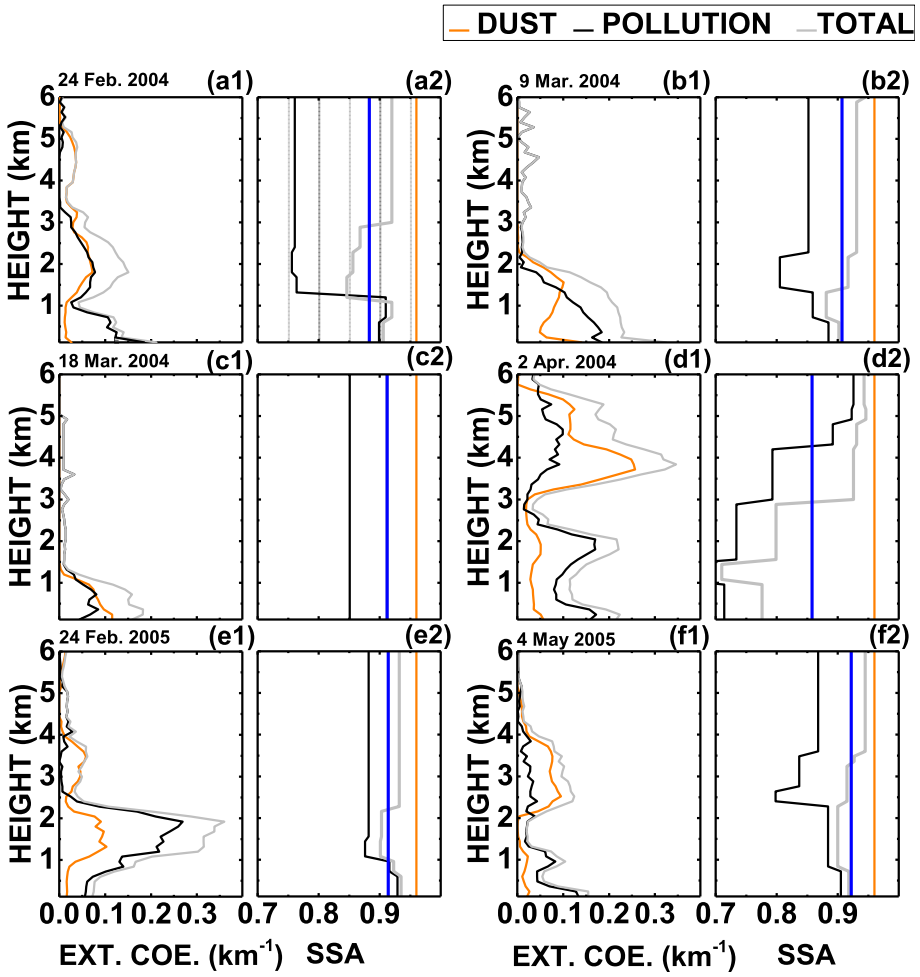

Fig. 1. Extinction coefficient (1) and single-scattering albedo (2) at 532 nm for dust (orange color), pollution (black color), and total (dust + pollution; gray color). The column-integrated single-scattering albedo from surface to 6 km altitude is also shown in the figure as blue color. The total and column-integrated single-scattering albedo is the same in Fig. 1(c). Therefore, the column-integrated single-scattering albedo is only shown in Fig. 1(c). (For interpretation of the references to color in this figure legend, the reader is referred to the web version of this article.)

carried out after sunset, the SSA profiles used in this study are obtained under nighttime conditions. However, the calculations of aerosol radiative forcing were performed separately for aerosol-laden and aerosol-free conditions at 12:00 local time. Thus, ADRF calculated in this study represents instantaneous ADRF at local noon time. Aerosol direct radiative forcing (ADRF) at the TOA and at the surface (SF) is calculated as follows:

$$\Delta F_{TOA} = NF^{a}_{TOA} - NF^{0}_{TOA} \quad (5)$$

$$\Delta F_{SF} = NF^{a}_{SF} - NF^{0}_{SF} \quad (6)$$

$$NF_{TOA} = F^{\downarrow}_{TOA} - F^{\uparrow}_{TOA} \quad (7)$$

$$NF_{SF} = F^{\downarrow}_{SF} - F^{\uparrow}_{SF} \quad (8)$$

The term ΔF denotes the aerosol direct radiative forcing, and NF^{a} and NF^{0} are the net flux for aerosol-laden and aerosol-free conditions, respectively. F↓ and F↑ are the downward and upward welling fluxes, respectively. The net flux change between TOA and surface is the flux absorbed in the layer. The heating rate is determined by the vertical divergence of the net radiative flux density (e.g., Hobbs, 2000):

$$\frac{\partial T}{\partial t} = \frac{g}{c_p} \cdot \frac{\Delta F}{\Delta P} \quad (9)$$

where $\partial T/\partial t$ is the heating rate (K/day), g is the acceleration due to gravity, C_p is the specific heat capacity of air at constant pressure and ΔP is the atmospheric pressure, respectively.

3. Radiative forcing Calculations

3.1. Radiative effect of mixed dust/anthropogenic pollution plumes

Aerosol direct radiative forcing (ADRF) and heating rates in the solar spectral region (0.25–4.0 μm) were calculated using SBDART. ADRF and heating rates were calculated for dust and anthropogenic pollution separately, and for the total case that dust and anthropogenic pollution are mixed. The vertical profile of extinction and SSA in Fig. 1 are used for dust and anthropogenic pollution calculations. In the latter case extinction coefficients are the same as in the case "total" in Fig. 1 but we used two cases of SSA data for the calculation. One is the profile of $SSA_{\mathbf{T}}$ and the other is the column-integrated SSA ($SSA_{\mathbf{int}}$).

We first investigated ADRF and heating rate of dust and anthropogenic pollution, respectively. Fig. 2(a1–d1) shows aerosol

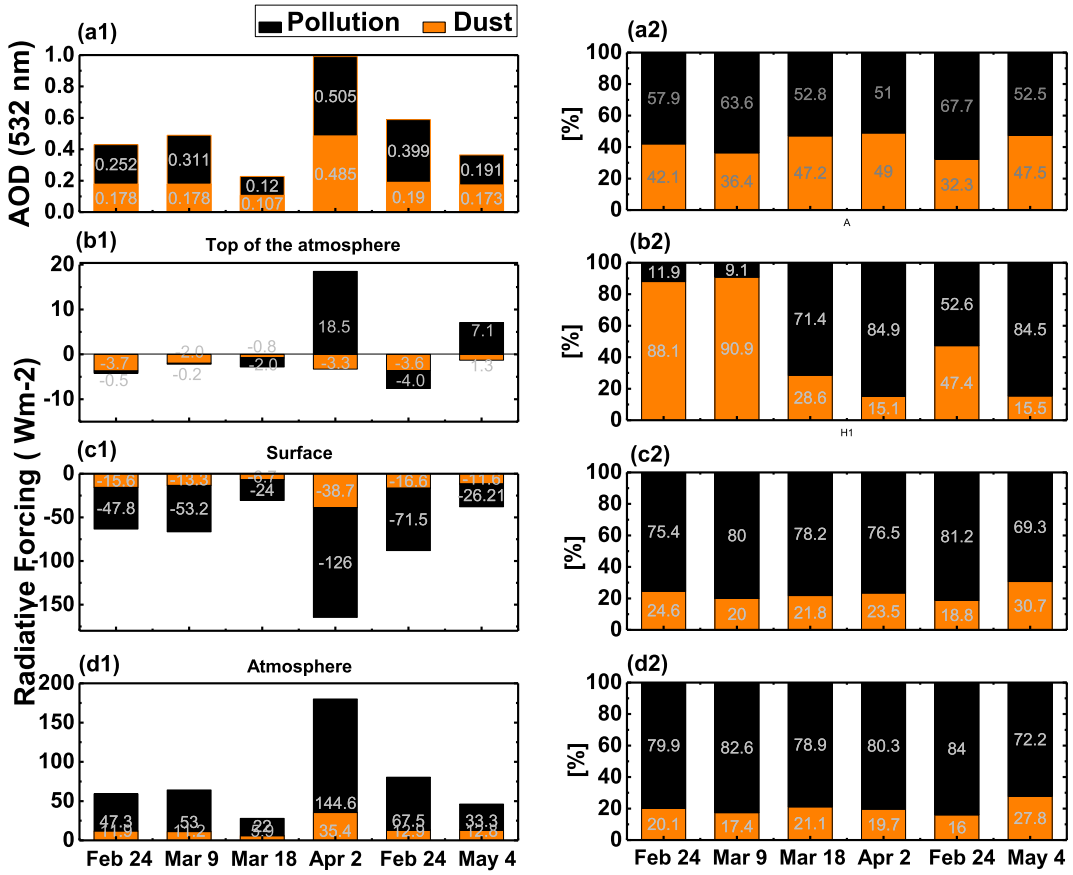

Fig. 2. Contribution of dust and pollution particles optical depth to combined (dust + pollution) aerosol optical depth (a), ADRF at the top of the atmosphere (b), at the surface (c), and in the atmosphere (d). Figures on the left (1) show the absolute values. Figures on the right (2) show the percentage contribution.

optical depths (a1) and direct radiative forcing at the TOA (b1), at the surface (c1), and in the atmosphere (d1) for dust and pollution, respectively. The highest total AOD of 0.99 and the lowest AOD of 0.227 were observed on 2 April and 18 March 2004, respectively.

The TOA radiative forcing of anthropogenic pollution shows negative values of −0.5, −0.2, −2.0, and −4.0 Wm^{-2} on 24 Feb, 9 and 18 Mar 2004, and 24 Feb 2005, respectively. Positive values of 18.5 and 7.1 Wm^{-2} are found on 2 Apr 2004 and 4 May 2005, respectively. The TOA radiative forcing of dust shows negative values for six cases. It means that more solar radiation is scattered back to space in the presence of dust particles which are slightly-absorbing aerosols (SSA = 0.96 at 532 nm). The magnitude of the forcing by dust and anthropogenic pollution aerosols at the surface is substantially larger than that at the TOA because of aerosol absorption in the atmosphere.

Fig. 2 (a2) shows the percent contributions of aerosol optical depth of dust and anthropogenic pollution aerosols, respectively, to combined (dust + pollution) aerosol optical depths. Fig. 2 (b2–d2) shows the percent contributions of dust and anthropogenic pollution ADRF to combined (dust + pollution) ADRF at TOA, at the surface, and in the atmosphere, respectively. The combined ADRF is calculated by just adding dust and anthropogenic pollution ADRF. The percent contributions to AOD by dust and anthropogenic pollution aerosol are 32.3–47.5% and 51.0–67.7%, respectively. Both, dust and anthropogenic pollution particles deplete the net solar radiation at the surface because of the combination of back-scattering and absorption of downwelling solar radiation. The contribution of anthropogenic pollution to this reduction is much higher than that the contribution caused by dust. We find 69.3–81.2% contribution of pollution aerosol ADRF to combined ADRF at the surface. The contribution of dust ADRF to combined ADRF is 18.8–30.7% at the surface. We find 72.2–84.0% and 16.0–27.8% contribution in the atmosphere for anthropogenic pollution and dust particles ADRF to combined ADRF, respectively. These numbers show that anthropogenic pollution aerosol contributes more to the ADRF at the surface and in the atmosphere, compared to the contribution to ADRF by dust. We assume that this high contribution by anthropogenic pollution is the result of its high light-absorption capacity. The largest percentage difference between contribution to ADRF by anthropogenic pollution and dust aerosols was observed on 2 Apr 2004. The low column-integrated SSA of 0.77 at 532 nm of anthropogenic pollution aerosols on that day demonstrates the effect light-absorption has on increasing radiative forcing.

Unlike the ADRF at the surface and in the atmosphere, the contribution of dust ADRF to the combined ADRF at the TOA is higher than 40% on 24 Feb and 9 Mar 2004, and 24 Feb 2005. Higher (closer to zero) and in part positive ADRFs at TOA for anthropogenic pollution were found for the cases shown in Fig. 2 (b-1). These results can be explained on the basis of the vertical distribution of anthropogenic pollution particles. AOD was 0.12 for anthropogenic pollution particle on 18 Mar 2004 and thus lowest of all AODs considered in this study. We find a low radiative forcing of −2.0 Wm^{-2}. Pollution particles are found below 1 km altitude on that day. Lowest ADRF of −4.0 Wm^{-2} compared to all other values at the TOA, was found on 24 Feb 2005. On that day anthropogenic pollution was located below 2 km altitude.

In contrast, TOA radiative forcing is higher for the case in which anthropogenic pollution with high extinction coefficients is located above 3 km altitude. This was the case on 2 Apr 2004 and 4 May

2005. Johnson et al. (2008) explain this effect by light-absorbing (biomass burning) aerosols. If absorbing particles are located at high altitude and if AOD is high, absorption of light scattered by molecules seems to be higher than in the case that pollution is at low altitude.

The vertical distribution of dust particles also affects the radiative effect at the TOA. Comparably low ADRFs are shown in Fig. 2. Low ADRFs are linked to cases of a high concentration of dust particles above 2 km altitude on 2 Apr 2004 and 4 May 2005. However, the impact of the vertical distribution on ADRF is less for dust aerosols compared to anthropogenic pollution aerosols. Meloni et al. (2005) reports that the radiative forcing caused by low-absorbing absorbing is weakly dependent on the vertical profile of these particles.

Since the observation date for each lidar measurement is different, we also have to consider the effect of the solar zenith angle on radiative forcing at the TOA. The solar zenith angle was at 46.53° (24 Feb 2004), 41.19° (9 Mar 2004), 37.61° (18 Mar 2004), 31.64° (2 Apr, 2004), 46.25° (24 Feb 2005), and 20.73° (4 May 2005). At the TOA, the upwelling radiation strongly depends on the aerosol phase function, which in turn depends on particle size. Large particles show a strong scattering peak in the forward direction (Meloni et al., 2005). As the solar zenith angle increases, a larger portion of the forward hemisphere includes the region of the upwelling scattered irradiance, and the radiative forcing decreases (more negative value) for solar zenith angles up to 70° (Keil et al., 2001; Meloni et al., 2005).

Fig. 3 shows ADRF profiles for dust and anthropogenic pollution aerosols. The vertical shape of the extinction profile (see Fig. 1) changes the vertical distribution of the ADRF. The ADRF becomes increasingly negative as the downward welling solar radiation encounters the aerosol layer. For an elevated aerosol layer above 3 km, this effect is seen at high altitude.

Since pollution particles are more absorbing than dust they are more efficient per unit AOD at reducing solar radiation at the surface and increasing absorption in the atmosphere. In contrast, dust particles are more efficient at decreasing the TOA solar flux. Fig. 4 shows the radiative effect of aerosol absorption. Fig. 4 (a1–f1) shows the vertically-resolved percentage ratio of the heating rate caused by dust and anthropogenic pollution, respectively. The vertical distribution of the percentage ratio of the dust-heating rate shows is similar in shape to the profile of the dust extinction coefficient, see Fig. 1.

Fig. 4 (a2–f2) and (a3–f3) represent the percentage ratio of the vertically-resolved extinction coefficients and absorption coefficients contributed by dust and anthropogenic pollution, respectively. The absorption coefficients were calculated from the extinction coefficients by multiplying the extinction coefficients by (1-SSA). The percentage ratio of the dust extinction coefficients is different from the percentage ratio of the dust heating rates at all altitudes. However, the percentage ratio of the absorption coefficient matches well the percentage ratio of the heating rate. This result can be considered as evidence for the effect of aerosol absorption on the radiative effect of aerosols. A higher percentage of ADRF at the surface and in the atmosphere Fig. 2 (c-2 and d-2) can be explained by Fig. 4.

3.2. Effect of vertical absorption property

In the previous sections we discussed the radiative effect of each dust and pollution if these two components are separated. The extinction coefficient is an extensive property which means that

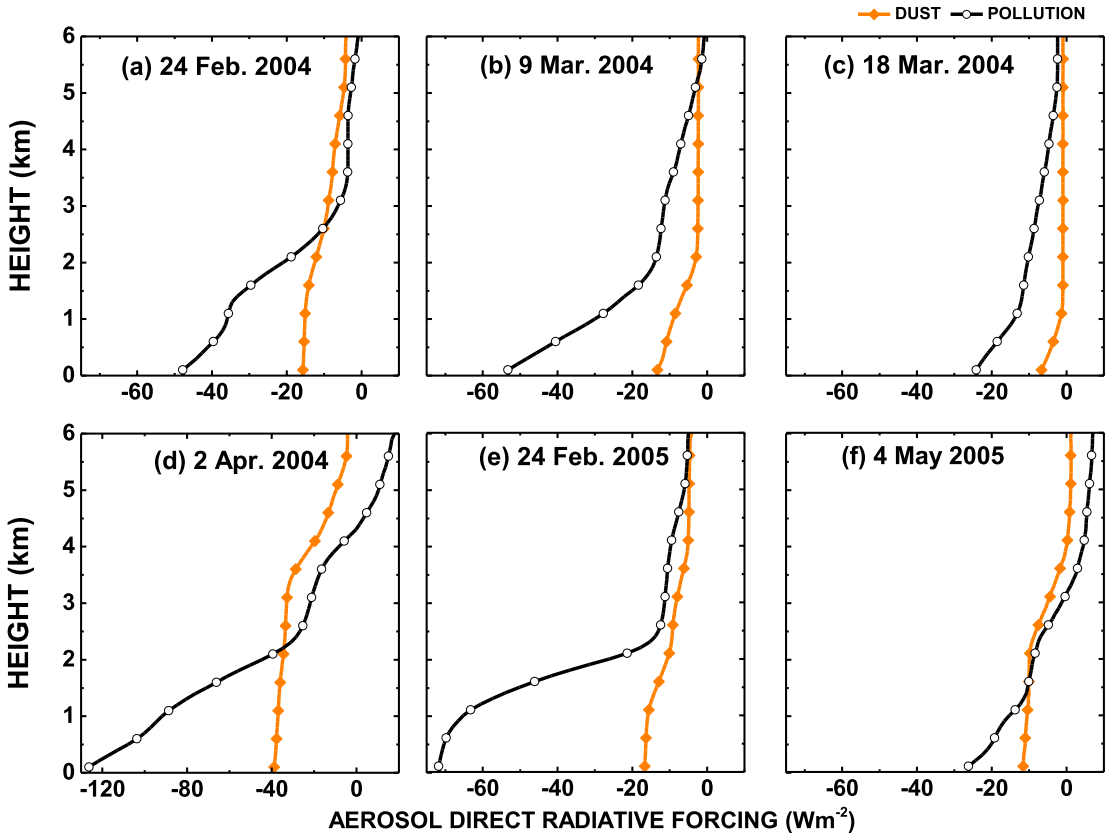

Fig. 3. Vertical resolved aerosol direct radiative forcing. The values for dust are expressed as orange color and pollution is black color. (For interpretation of the references to color in this figure legend, the reader is referred to the web version of this article.)

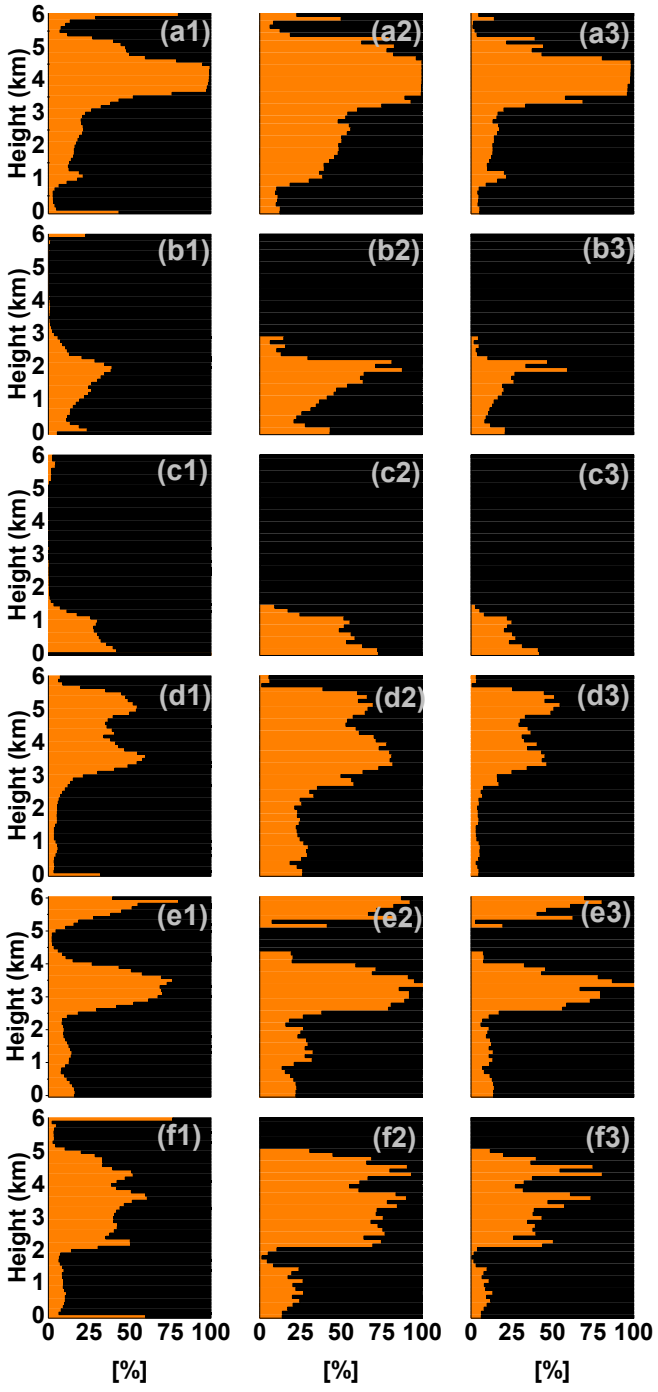

Fig. 4. Vertical resolved percentage contribution between dust (orange color) and pollution (black color) for heating rate (1), aerosol extinction coefficient at 532 nm (2), and aerosol absorption coefficient at 532 nm (3) on 24 February (a), 9 March (b), 18 March (c), and 2 April 2004 (d), and on 24 February (e) and 4 May 2005 (f). (For interpretation of the references to color in this figure legend, the reader is referred to the web version of this article.)

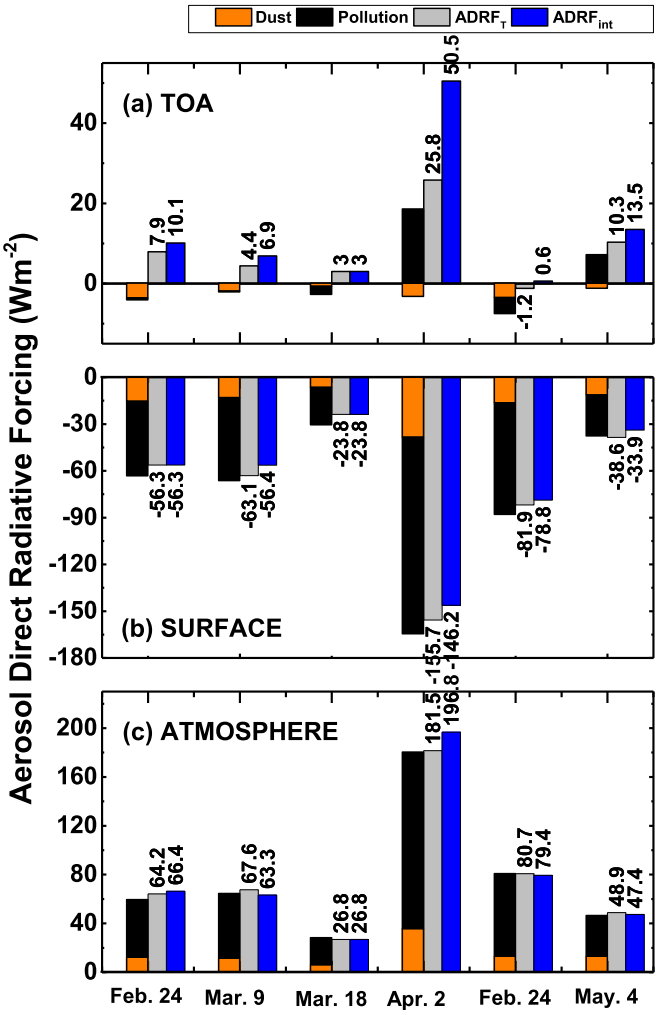

Fig. 5. ADRF at the TOA (a), at the surface (b), and in the atmosphere (c) for the vertical profile of SSA_T is applied (gray color) and column-integrated SSA is applied (blue color) cases. The stacked ADRF of dust (orange color) and pollution (black color) is also shown in the figure. (For interpretation of the references to color in this figure legend, the reader is referred to the web version of this article.)

total extinction of a mixed dust/pollution plume can simply be computed by adding extinction by dust and extinction by anthropogenic pollution. However, the SSA is an intensive property, i.e. SSA of a mixed dust/pollution plume does not follow from adding SSA of dust to SSA of anthropogenic pollution. In the same way it is not reasonable to compute radiative forcing of a mixed dust/pollution plume by simply adding the radiative forcing caused by dust to radiative forcing caused by anthropogenic pollution. For that reason we calculated SSA_T as explained in section 2.1. The ADRF and heating rates of the total (dust + pollution) aerosol layer were calculated using SSA_T. It is denoted as $ADRF_T$. In the other case we use the column-integrated SSA_{int} for the calculations ($ADRF_{int}$). The same profiles of total (dust + pollution) extinction coefficients were used in both cases.

Fig. 5 shows $ADRF_T$ and $ADRF_{int}$ at the TOA, at the surface, and in the atmosphere for the cases of using SSA_T and SSA_{int}, respectively. Fig. 5 also includes the stacked ADRFs of separately-calculated dust and anthropogenic pollution shown in Fig. 2 (b-1, c-1, and d-1). With regard to the conditions at the surface and in the atmosphere $ADRF_T$ and $ADRF_{int}$ are similar to the stacked cases. However, at TOA the $ADRF_T$ and $ADRF_{int}$ of the mixed dust/pollution plume are positive, which is in contrast to the values of the individual ADRFs of dust and pollution. Johnson et al. (2008) reported this kind of increase of ADRF when dust was included as part of the background particles. Since more solar radiation is reflected upward by the dust by backscattering, the upwelling fluxes will increase through the atmosphere and the absorption effect of pollution increases (Johnson et al., 2008). Keil et al. (2001) also report that the negative TOA solar radiative forcing of aerosol particles significantly decreases (to zero or even positive values) when the position of

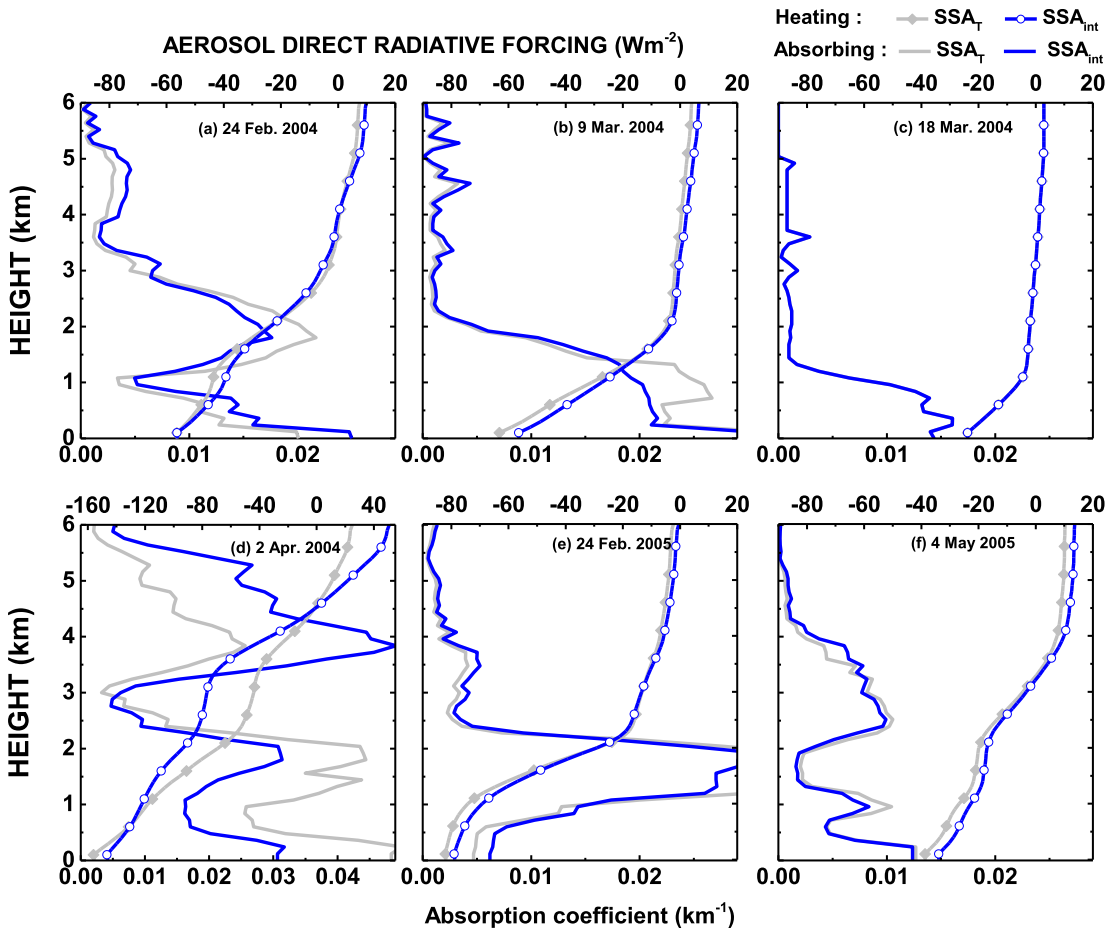

Fig. 6. Vertical resolved aerosol absorption coefficient at 532 nm (line) and aerosol direct radiative forcing (line and symbol). The value for the vertical profile of SSA_T applied case is expressed as gray color and the column-integrated SSA applied case is shown as blue color. Since the input parameters are the same for the total and column-integrated cases on March 18, 2004, the same value is calculated. For that reason, only the blue color is shown in Fig. 6 (c). (For interpretation of the references to color in this figure legend, the reader is referred to the web version of this article.)

absorbing layers expressed in terms of the altitude information is included in the radiative forcing calculations.

While scattering processes in the atmosphere control which portion of the incoming radiation is scattered back to space, absorption transfers the light to other energy forms, mainly heat (Keil et al., 2001). Thus an increasing burden of scattering particles (e.g., sulfates) induces a net cooling effect (Charlson et al., 1991; Keil et al., 2001). If absorbing aerosols are present in the atmosphere, this cooling can be reduced or even changed into a heating (Chýlek and Coakley, 1974; Haywood and Shine, 1995; Keil et al., 2001; Johnson et al., 2008). The positive value of radiative forcing at the TOA for the $ADRF_T$ and $ADRF_{int}$ cases can be explained by these processes.

Although the positive values of radiative forcing were calculated at the TOA for $ADRF_T$ and $ADRF_{int}$, the $ADRF_{int}$ cases showed higher values than the $ADRF_T$ cases except for the results we obtain for 18 Mar 2004. The values between $ADRF_T$ and $ADRF_{int}$ were the same on 18 Mar 2014 because the same values were used as input parameters.

Although the absorption capacity when integrated from surface to 6 km altitude is the same for the case of SSA_T and SSA_{int} cases, the absorption profiles for these two cases are different, see Fig. 1. Fig. 6 shows the vertically resolved absorption coefficient and $ADRF_T$ and $ADRF_{int}$ that follow from using SSA_T and SSA_{int} in the computations, respectively. The absorption coefficients obtained from using SSA_{int} are higher than the absorption coefficients obtained from using SSA_T above 2–3 km altitude. $ADRF_{int}$ is also higher than $ADRF_T$ at 6 km altitude. This result shows that the radiative effects in the solar wavelength region are sensitive to the vertical profile of aerosol absorption, although the magnitude of the variation is related to the concentration of aerosol particles.

The ADRF values at the TOA in this study are a good example for the variation of ADRF caused by multi-aerosol layers with different absorbing properties. A simple explanation is that when the scattering-dominating aerosol layer is beneath the absorption-dominating aerosol layer the amount of solar radiation that is scattered up into the absorbing layer increases. This would increase the absorption of solar radiation by the absorbing aerosol. When the scattering-dominating aerosol layer is above the absorption-dominating aerosol layer it will shadow the absorbing layer, thus reducing absorption of solar radiation by the absorbing aerosol.

ADRF of 50.5 Wm^{-2} at the TOA for the $ADRF_{int}$ case is higher than 25.8 Wm^{-2} we find for the $ADRF_T$ case on 2 Apr 2004. Although the dust-dominated aerosol layer stretches from 3 to 6 km altitude, the absorption coefficients for SSA_{int} is higher than SSA_T at that height. We find higher value for the $ADRF_{int}$ cases compared to the $ADRF_T$ cases on all days except 18 Mar 2004. We assume that this result is caused by the difference of the SSA of aerosol layers above 3 km altitude.

Fig. 7 shows the heating rates for dust, pollution, and just summed value of the dust and anthropogenic pollution. The heating rates of the total (dust + pollution) aerosol layer calculated

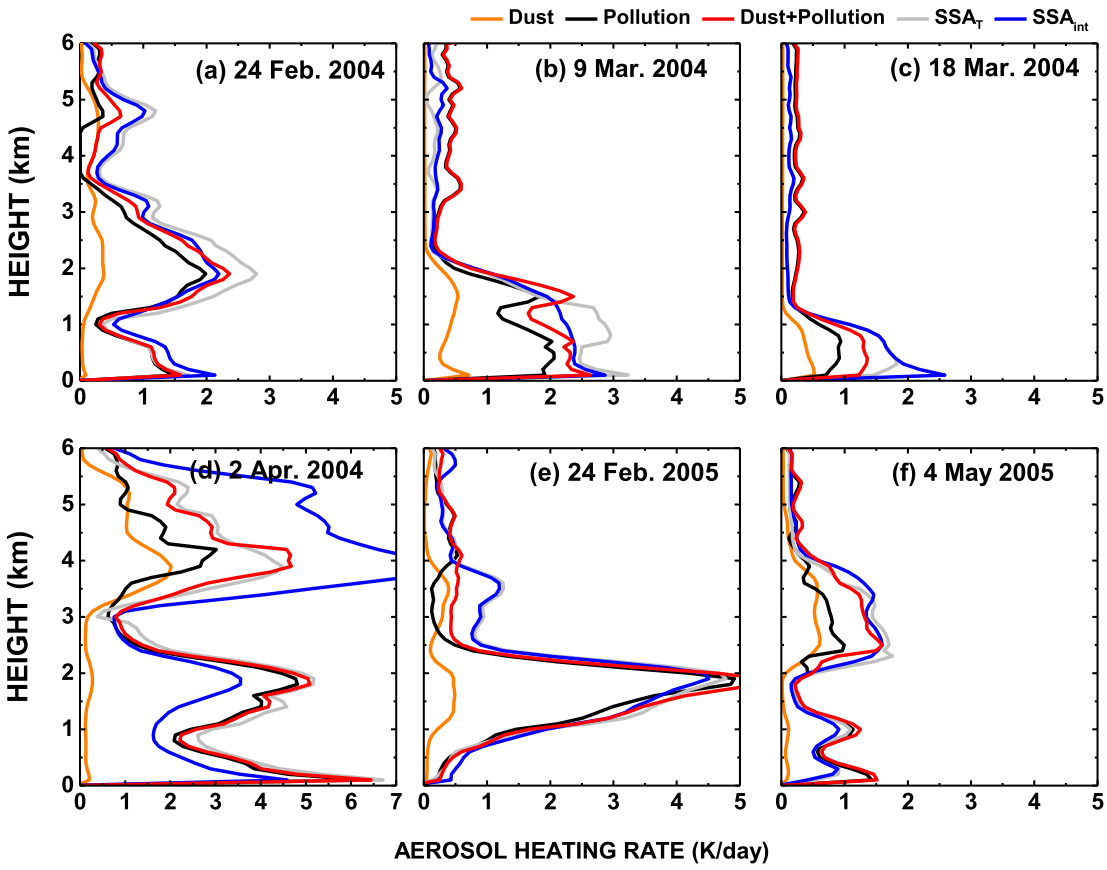

Fig. 7. Profiles of heating rate for dust (orange), pollution (black), total (dust + pollution) with vertical profile of SSA (gray), and total with column averaged SSA (blue). The summed value of dust and pollution is denoted as red color. (For interpretation of the references to color in this figure legend, the reader is referred to the web version of this article.)

using SSA_T and SSA_{int} are also shown in Fig. 7. The vertical distribution of the heating rates is similar to the vertical profiles of the extinction coefficient shown in Fig. 1. The heating rate of dust particles is smaller compared to the heating rate of pollution particles, which demonstrates that the energy absorption efficiency of dust particles is smaller than that of pollution particles. The values of the total aerosol layer using SSA_T and SSA_{int} are similar to the summed value of the dust and anthropogenic pollution.

Noh et al. (2012) report that pollution particles within mixed dust layers are considered to play a significant role in the increase of the radiative heating rate, which in turn may lead to a self-sustaining mechanism such that long-range transport of dust plumes is possibly extending because of the increased static stability of dust layers. Since column-integrated SSA retrieved by AERONET sun/sky radiometer was used in that study, the effect might be overestimated or underestimated. In conclusion, our results in this study shows that air masses containing a mix of dust and pollution particles may lead to longer transport distances of dust particles because the enhanced light-absorption capacity of light-absorbing pollution particles leads to increased heating rates.

3.3. Sensitivity test for different absorption property layers

We simulated solar radiative forcing in order to find out whether the vertical variability of aerosol absorption properties in mixed dust/pollution layers has any significant impact on the shortwave radiative budget in a cloud-free atmosphere. The impact of the vertical distribution of atmospheric aerosols on radiative forcing has been studied by e.g. Keil et al. (2001), Meloni et al. (2005), Johnson et al. (2008), Guan et al. (2010), Vuolo et al. (2014), Feng et al. (2016), and Mishra et al. (2015). However, studies that simultaneously consider multiple aerosol layers with different light-absorption properties in each layer, like the case of 2 April 2004, have not been carried out yet. We simulated solar radiative forcing caused by a dual-layered structure in which an elevated mixed dust/pollution layer is located between 3 and 5 km height above ground, i.e., in the free troposphere (**FF**), and a second layer is located below 2 km height above ground, i.e., within the boundary layer (**WBL**). This double-layer has different dust ratios in the **FF** and the **WBL**. If the ratio in the **WBL** is composed of 20% dust particles and 80% pollution particles, and **FF** is composed of 80% dust particles and 20% pollution particles, it is denoted as Dr_{20}. The percentages are related to the optical depths in the FF and the WBL.

We simulated seven types of mixed-dust layers from Dr_{20} to Dr_{80} by increasing the dust concentration by 10% from one case to the next case. The SSAs of pure dust and anthropogenic pollution

Table 1
Dust ratio within boundary layer and free troposphere and those single-scattering albedo for each layer.

	Dust ratio (%)		SSA (532 nm)		
	WBL	FF	WBL	FF	Column averaged
D_{r20}	20	80	0.752	0.908	0.83
D_{r30}	30	70	0.778	0.882	0.83
D_{r40}	40	60	0.804	0.856	0.83
D_{r50}	50	50	0.83	0.83	0.83
D_{r60}	60	40	0.856	0.804	0.83
D_{r70}	70	30	0.882	0.778	0.83
D_{r80}	80	20	0.908	0.752	0.83

WBL: Within boundary layer (W, 0–2 km); FF: In the free troposphere (F, 3–5 km).

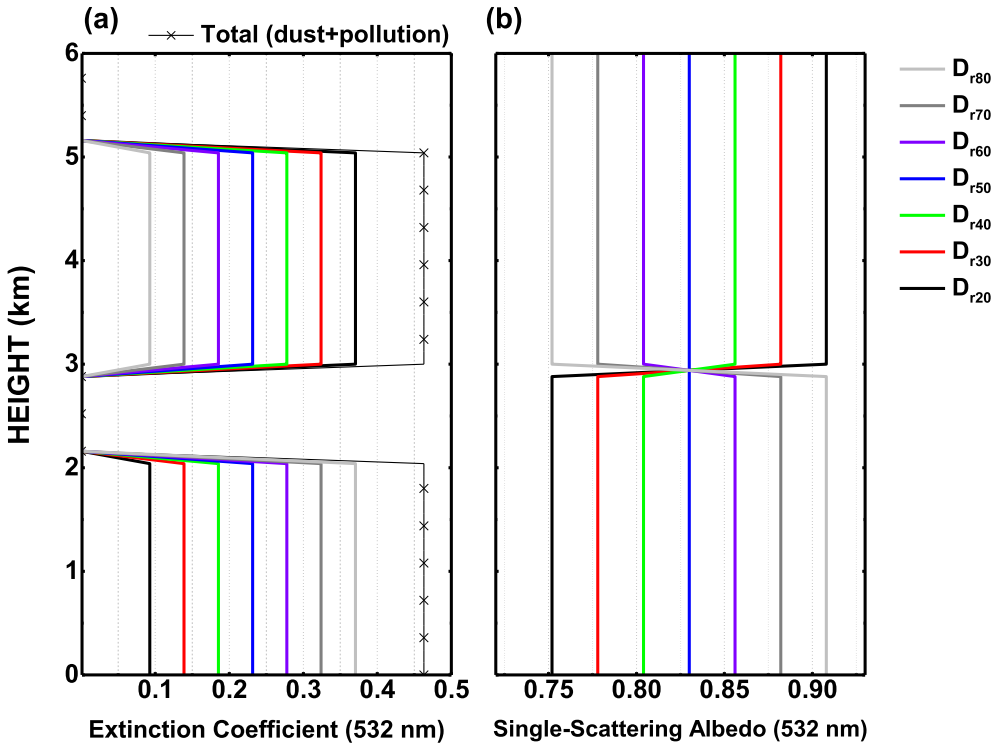

Fig. 8. (a) Simulated vertical distribution of dust extinction coefficient at 532 nm. If 20% dust is present for lower mixed layer, 80% of dust exists above mixed layer. Rest part is composed of pollution in each mixed layer. The combined extinction coefficient with dust and pollution is denoted as thin black line and '×' symbol. (b) The total SSA of each mixed-dust layer is shown according to different dust ratio.

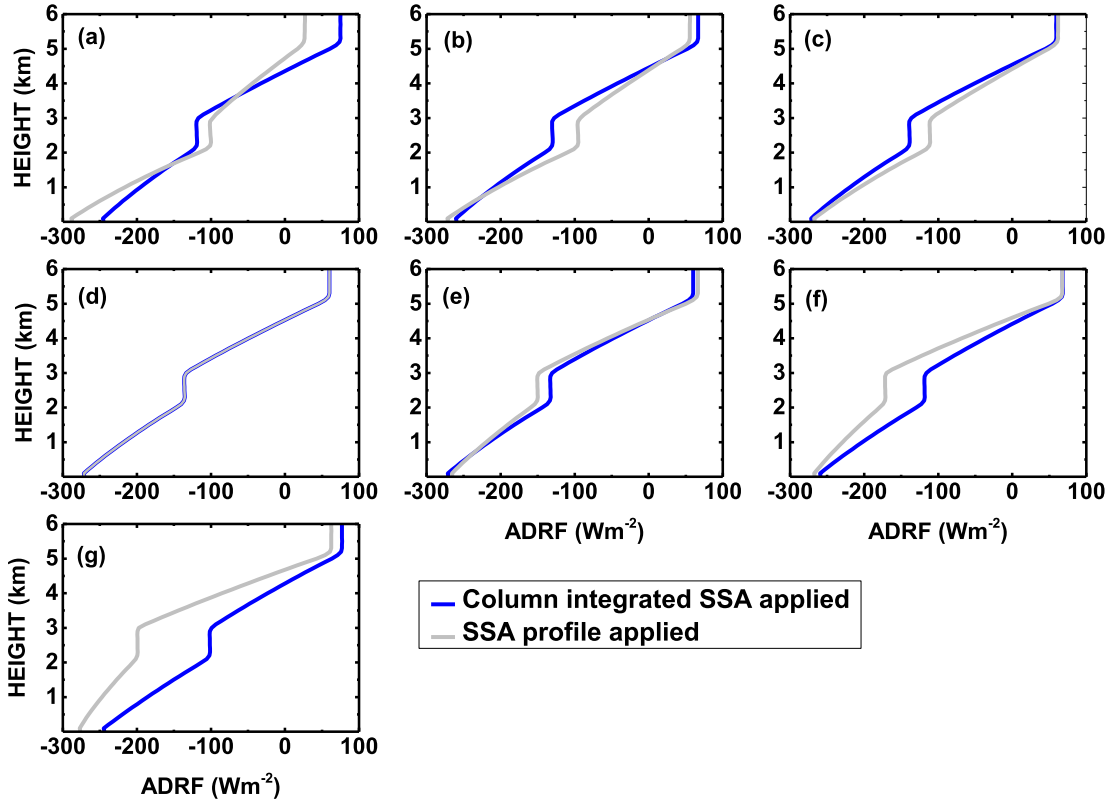

Fig. 9. Simulation results of vertical resolved aerosol direct radiative forcing for profile applied SSA (gray) and column integrated SSA (blue) cases. (For interpretation of the references to color in this figure legend, the reader is referred to the web version of this article.)

are assumed as 0.96 and 0.70 at 532 nm, respectively. Based on these SSA values, we calculated the SSA for **FF** and **WBL** according to equation (3), see section 2.1. The column-integrated SSA is also calculated with the method shown in equation (4). The column-integrated SSA that describes the combined effect of the **WBL** and the **FF** is 0.83 at 532 nm for all seven dust ratio cases. The dust ratios and values of the SSA of each layer of these seven types of mixed dust/pollution layers are explained in Table 1.

Fig. 8 (a) shows the contribution of dust to the extinction coefficients in the mixed dust/pollution plume for each of the seven types. Although the ratio of dust varies from 20 to 80% in each of the seven cases, the AOD of each **WBL** and **FF** layer (dust plus pollution) is 1 at 532 nm, thus the total column-integrated AOD from surface to 6 km altitude is 2. Fig. 8 (b) shows the SSA of each **WBL** and **FF** layer for each seven cases. The differences of SSA between **WBL** and **FF** are largest for the case Dr_{20}. The differences decrease until the case Dr_{50} is reached. The differences increase again for the case Dr_{60} and the following cases.

Fig. 9 shows the simulation results of the ADRF profiles for the case that the column-integrated SSA was used and for the case that profiles of the SSA were used. Fig. 10 shows the ADRFs at the TOA, at the surface, and in the atmosphere for the case that the column-integrated SSA was used and for the case that profiles of the SSA were used.

The ADRFs at the surface and in the atmosphere show similar values for the different cases of dust ratios if profile-information of SSA is used in the computations. The differences of the ADRFs obtained from using profile information of the SSA and column-integrated values of the SSA are small at the surface and in the atmosphere. We find comparable large differences at the surface between the case Dr_{20} and Dr_{80}. The ADRF is -287.3 Wm^{-2} and thus the lowest of all values obtained in our simulations. We find a comparable large difference of 42.3 Wm^{-2} between the case of using profile-information of the SSA and using column-averaged values of the SSA at the surface for the case Dr_{20}.

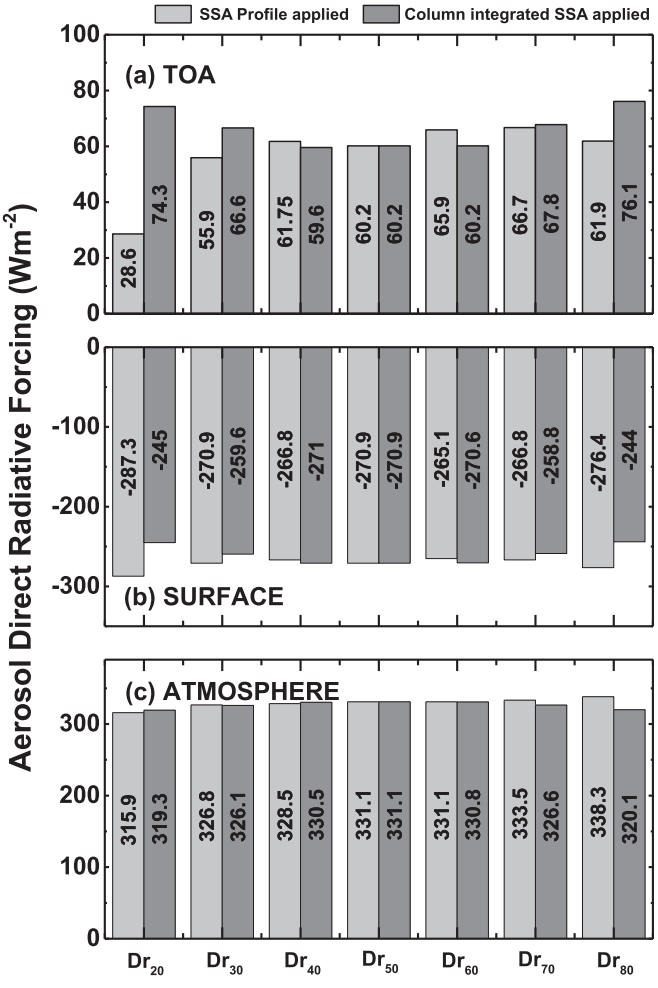

Fig. 10. ADRF at the TOA (a), at the surface (b), and in the atmosphere (c) for the profile applied SSA (light gray) and column integrated SSA (gray) cases.

Fig. 10(a) shows that the ADRF at the TOA differ from each other significantly in dependence of the dust ratios. The lowest ADRF of 28.6 Wm^{-2} is obtained for the case Dr_{20} if profile information of the SSA is used in the computations. The ADRF increases with increasing dust ratio (cases Dr_{20} to Dr_{70}). With respect to Dr_{20} there are large differences of the ADRF at the TOA between the case of using the column-averaged SSA or the profile of the SSA. This difference becomes less with increasing dust ratio up to Dr_{50}. The difference then increases again from Dr_{60} to Dr_{80}. These results can be explained by the difference of SSA between **WBL** and **FF**. Although the AOD is 1 for each of the mixed dust layers, the light absorption property of each layer is different. The SSA of **WBL** and **FF** is 0.752 and 0.908 in the case of Dr_{20}. If the dust ratio increases the SSA of WBL decreases and the SSA of FF is increases. The absorbing aerosols strongly absorb the radiation scattered by the molecules in the air, which significantly alters the backscattered radiation at the TOA (Torres et al., 1998; Mishra et al., 2015). Absorbing aerosols at higher altitudes will interact stronger with the upward fraction of the radiation scattered by the molecules. For that reason, the backscattered radiance at TOA caused by an aerosol layer located at high altitude is less than that backscattered radiance at TOA caused by an aerosol layer at low altitude if the same amount of aerosol exists in the atmosphere (Mishra et al., 2015). In contrast, in cases where a scattering-dominant aerosol layer is at high altitude, most of the incoming radiation will first backscatter to the TOA before it can be absorbed in the atmosphere. The heating rate profiles shown in Fig. 11 can explain the effect of aerosol absorption in dependence of altitude of the aerosol layer. Although the same extinction coefficients and SSAs are used, the effect of absorption is larger for the FF case than for the WBL case. WBL in Fig. 11 (a) and FF in Fig. 11 (g) have the same extinction coefficient and SSA, but the heating rate in the FF (Fig. 11 (g)) is much higher than the heating rate in the WBL (Fig. 11 (a)).

4. Summary and conclusions

The direct aerosol radiative forcing and heating rates of mixed-dust pollution plumes were estimated using vertical profiles of aerosol extinction coefficients and single-scattering albedos. The profiles were obtained from data taken with a multi-wavelength Raman lidar system in South Korea. Four cases of radiative forcing were calculated with the model SBDART: 1. Dust, 2. pollution, 3. mixed-dust plume and the use of vertical profiles of SSA, and 4. mixed-dust plumes and the use of column-integrated values of the SSA.

The ADRF at the surface and in the atmosphere show a small dependence on the aerosol vertical profile and its light-absorption properties for all four cases. In contrast, at the TOA, the ADRF is largely affected by the vertical distribution of aerosols. As the altitude above ground of the aerosol layer increased, ADRF also increased. We find differences of the radiative effect of two-layer aerosol plumes if the light-absorption between the two layers differs. Although the absorption property and the vertical profile of the extinction coefficient of the aerosols are the same for the two-layered aerosol plume we find higher ADRF at the TOA if a strong light-absorbing aerosol layer is located at high altitude above

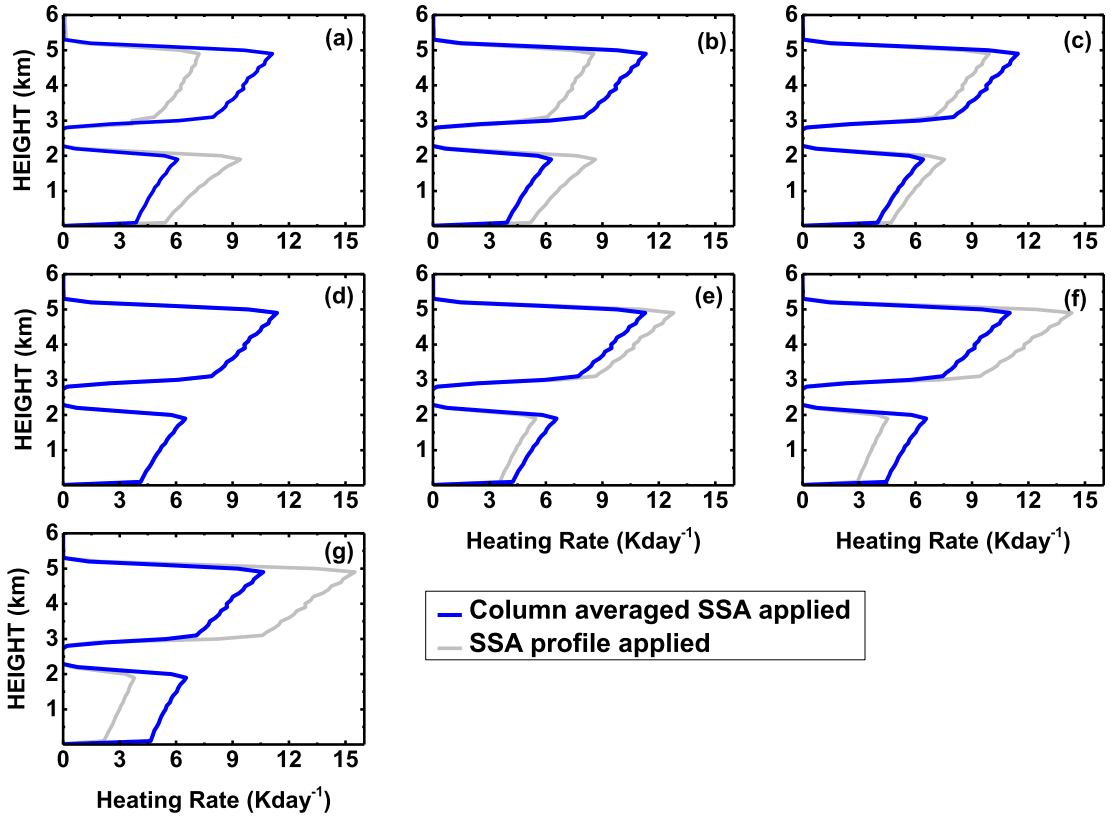

Fig. 11. Profiles of heating rate for the profile applied SSA (gray) and column integrated SSA (blue) cases.

ground. The ADRF at the TOA increases when the light-absorbing aerosol layer is located above 3 km altitude.

The differences that we obtain from using a vertically resolved SSA (can be obtained from using lidar data) and a total layer-mean SSA (can be obtained from using Sun/sky radiometer data) indicates that the interpretation of results obtained with Sun/sky radiometer data alone can be misleading as there might be large errors involved in the calculations of ADRF at the TOA and the vertical profiles of heating rates. Sensitivity tests with various dust ratios in two-layered pollution plumes reveal that a column-averaged SSA may induce large errors of ADRF at the TOA and vertical profiles of heating rates. The heating changes can in turn cause dynamical changes in the atmospheric circulation and stability (Shell and Somerville, 2007). For example, increased absorption of solar radiation within the atmosphere can result in atmospheric warming and surface cooling (Tegen et al., 1996; Ramanathan et al., 2007; Shell and Somerville, 2007). This redistribution of heating within the column affects the stability of the atmosphere, with implications for convection, latent heat transport, and precipitation (Shell and Somerville, 2007). For these reasons we have to be careful when we calculate the ADRF using column-integrated optical data obtained from remote sensing instruments like AERONET Sun/sky radiometers, especially if we consider cases of mixed-dust pollution plumes.

Acknowledgements

This work was funded by the Korea Meteorological Administration Research and Development Program under Grant KMIPA 2015-6150. This research was also supported by the International Environmental Research Center (IERC).

References

Arnott, W.P., Walker, J.W., Moosmüller, H., Elleman, R.A., Jonsson, H.H., Buzorius, G., Conant, W.C., Flagan, R.C., Seinfeld, J.H., 2006. Photoacoustic insight for aerosol light absorption aloft from meteorological aircraft and comparison with particle soot absorption photometer measurements: DOE Southern Great Plains climate research facility and the coastal stratocumulus imposed perturbation experiments. J. Geophys. Res. 111 http://dx.doi.org/10.1029/2005JD005964.

Bellouin, N., Jones, A., Haywood, J., Christopher, S.A., 2008. Updated estimate of aerosol direct radiative forcing from satellite observations and comparison against the Hadley Centre climate model. J. Geophys. Res. 113 http://dx.doi.org/10.1029/2007JD009385.

Bergstrom, R.W., Pilewskie, P., Russell, P.B., Redemann, J., Bond, T.C., Quinn, P.K., Sierau, B., 2007. Spectral absorption properties of atmospheric aerosols. Atmos. Chem. Phys. 7, 5937–5943. http://dx.doi.org/10.5194/acp-7-5937-2007.

Charlson, R.J., Langner, J., Rodhe, H., Leovy, C.B., Warren, S.G., 1991. Perturbation of the northern hemisphere radiative balance by backscattering from anthropogenic sulfate aerosols*. Tellus A 43, 152–163. http://dx.doi.org/10.1034/j.1600-0870.1991.00013.x.

Chýlek, P., Coakley, J.A., 1974. Aerosols and climate. Science 183, 75–77. http://dx.doi.org/10.1126/science.183.4120.75.

Dubovik, O., Holben, B., Eck, T.F., Smirnov, A., Kaufman, Y.J., King, M.D., Tanré, D., Slutsker, I., 2002. Variability of absorption and optical properties of key aerosol types observed in worldwide locations. J. Atmos. Sci. 59, 590–608. http://dx.doi.org/10.1175/1520-0469(2002)059. <0590:VOAAOP>2.0.CO;2.

Eck, T.F., Holben, B.N., Reid, J.S., O'Neill, N.T., Schafer, J.S., Dubovik, O., Smirnov, A., Yamasoe, M.A., Artaxo, P., 2003. High aerosol optical depth biomass burning events: a comparison of optical properties for different source regions. Geophys. Res. Lett. 30 (20), 2035. http://dx.doi.org/10.1029/2003GL017861.

Eck, T.F., Holben, B.N., Dubovik, O., Smirnov, A., Goloub, P., Chen, H.B., Chatenet, B., Gomes, L., Zhang, X.-Y., Tsay, S.-C., Ji, Q., Giles, D., Slutsker, I., 2005. Columnar aerosol optical properties at AERONET sites in central eastern Asia and aerosol transport to the tropical mid-Pacific. J. Geophys. Res. Atmos. 110, D06202. http://dx.doi.org/10.1029/2004JD005274.

Eck, T.F., Holben, B.N., Sinyuk, A., Pinker, R.T., Goloub, P., Chen, H., Chatenet, B., Li, Z., Singh, R.P., Tripathi, S.N., Reid, J.S., Giles, D.M., Dubovik, O., O'Neill, N.T., Smirnov, A., Wang, P., Xia, X., 2010. Climatological aspects of the optical properties of fine/coarse mode aerosol mixtures. J. Geophys. Res. 115, D19205. http://dx.doi.org/10.1029/2010JD014002.

Feng, Y., Kotamarthi, V.R., Coulter, R., Zhao, C., Cadeddu, M., 2016. Radiative and thermodynamic responses to aerosol extinction profiles during the pre-

monsoon month over South Asia. Atmos. Chem. Phys. 16, 247–264. http://dx.doi.org/10.5194/acp-16-247-2016.
Gadhavi, H., Jayaraman, A., 2006. Airborne lidar study of the vertical distribution of aerosols over Hyderabad, an urban site in central India, and its implication for radiative forcing calculations. Ann. Geophys. 24, 2461–2470. http://dx.doi.org/10.5194/angeo-24-2461-2006.
Giles, D.M., Holben, B.N., Eck, T.F., Sinyuk, A., Smirnov, A., Slutsker, I., Dickerson, R.R., Thompson, A.M., Schafer, J.S., 2012. An analysis of AERONET aerosol absorption properties and classifications representative of aerosol source regions: aerosol absorption and classifications. J. Geophys. Res. Atmos. 117, D17203. http://dx.doi.org/10.1029/2012JD018127.
Guan, H., Schmid, B., Bucholtz, A., Bergstrom, R., 2010. Sensitivity of shortwave radiative flux density, forcing, and heating rate to the aerosol vertical profile. J. Geophys. Res. 115, D06209. http://dx.doi.org/10.1029/2009JD012907.
Haywood, J.M., Shine, K.P., 1995. The effect of anthropogenic sulfate and soot aerosol on the clear sky planetary radiation budget. Geophys. Res. Lett. 22, 603–606. http://dx.doi.org/10.1029/95GL00075.
Highwood, E.J., 2003. Radiative properties and direct effect of Saharan dust measured by the C-130 aircraft during Saharan Dust Experiment (SHADE): 2. Terrestrial spectrum. J. Geophys. Res. 108, 8578. http://dx.doi.org/10.1029/2002JD002552.
Hobbs, P.V., 2000. Introduction to Atmospheric Chemistry, 262. Cambridge Univ. Press, New York.
Huang, J., Fu, Q., Su, J., Tang, Q., Minnis, P., Hu, Y., Yi, Y., Zhao, Q., 2009. Taklimakan dust aerosol radiative heating derived from CALIPSO observations using the Fu-Liou radiation model with CERES constraints. Atmos. Chem. Phys. 9, 4011–4021. http://dx.doi.org/10.5194/acp-9-4011-2009.
Johnson, B.T., Heese, B., McFarlane, S.A., Chazette, P., Jones, A., Bellouin, N., 2008. Vertical distribution and radiative effects of mineral dust and biomass burning aerosol over West Africa during DABEX. J. Geophys. Res. 113, D00C12. http://dx.doi.org/10.1029/2008JD009848.
Keil, A., Wendisch, M., Brüggemann, E., 2001. Measured profiles of aerosol particle absorption and its influence on clear-sky solar radiative forcing. J. Geophys. Res. Atmos. 106, 1237–1247. http://dx.doi.org/10.1029/2000JD900486.
Levy, R.C., Remer, L.A., Mattoo, S., Vermote, E.F., Kaufman, Y.J., 2007. Second-generation operational algorithm: retrieval of aerosol properties over land from inversion of Moderate Resolution Imaging Spectroradiometer spectral reflectance. J. Geophys. Res. Atmos. 112, D13211. http://dx.doi.org/10.1029/2006JD007811.
Meloni, D., di Sarra, A., Di Iorio, T., Fiocco, G., 2005. Influence of the vertical profile of Saharan dust on the visible direct radiative forcing. J. Quantitative Spectrosc. Radiat. Transf. 93, 397–413. http://dx.doi.org/10.1016/j.jqsrt.2004.08.035.
Mishra, A.K., Klingmueller, K., Fredj, E., Lelieveld, J., Rudich, Y., Koren, I., 2014. Radiative signature of absorbing aerosol over the eastern Mediterranean basin. Atmos. Chem. Phys. 14, 7213–7231. http://dx.doi.org/10.5194/acp-14-7213-2014.
Mishra, A.K., Koren, I., Rudich, Y., 2015. Effect of aerosol vertical distribution on aerosol-radiation interaction: a theoretical prospect. Heliyon 1, e00036. http://dx.doi.org/10.1016/j.heliyon.2015.e00036.
Müller, D., Wandinger, U., Ansmann, A., 1999a. Microphysical particle parameters from extinction and backscatter lidar data by inversion with regularization: simulation. Appl. Opt. 38, 2358–2368. http://dx.doi.org/10.1364/AO.38.002358.
Müller, D., Wandinger, U., Ansmann, A., 1999b. Microphysical particle parameters from extinction and backscatter lidar data by inversion with regularization: Simulation. Appl. Opt. 38, 2358–2368.
Müller, D., Wagner, F., Wandinger, U., Ansmann, A., Wendisch, M., Althausen, D., von Hoyningen-Huene, W., 2000. Microphysical particle parameters from extinction and backscatter lidar data by inversion with regularization: experiment. Appl. Opt. 39, 1879–1892.
Müller, D., Mattis, I., Wandinger, U., Ansmann, A., Althausen, D., Stohl, A., 2003. Indo-Asian pollution during INDOEX: microphysical particle properties and single-scattering albedo inferred from multiwavelength lidar observations. J. Geophys. Res. 108, 4600. http://dx.doi.org/10.1029/2003JD003538.
Müller, D., Franke, K., Ansmann, A., Althausen, D., 2005. Raman lidar observations of aged Siberian and Canadian forest fire smoke in the free troposphere over Germany in 2003: microphysical particle characterization. J. Geophys. Res. 110, D17201. http://dx.doi.org/10.1029/2004JD005756.
Murayama, T., Müller, D., Wada, K., Shimizu, A., Sekiguchi, M., Tsukamoto, T., 2004. Characterization of Asian dust and siberian smoke with multi-wavelength Raman lidar over tokyo, Japan in spring 2003: Raman lidar observation of Asian dust and smoke. Geophys. Res. Lett. 31 http://dx.doi.org/10.1029/2004GL021105 n/a–n/a.
Myhre, G., Samset, B.H., Schulz, M., Balkanski, Y., Bauer, S., Berntsen, T.K., Bian, H., Bellouin, N., Chin, M., Diehl, T., Easter, R.C., Feichter, J., Ghan, S.J., Hauglustaine, D., Iversen, T., Kinne, S., Kirkevåg, A., Lamarque, J.-F., Lin, G., Liu, X., Lund, M.T., Luo, G., Ma, X., van Noije, T., Penner, J.E., Rasch, P.J., Ruiz, A., Seland, ø., Skeie, R.B., Stier, P., Takemura, T., Tsigaridis, K., Wang, P., Wang, Z., Xu, L., Yu, H., Yu, F., Yoon, J.-H., Zhang, K., Zhang, H., Zhou, C., 2013. Radiative forcing of the direct aerosol effect from AeroCom Phase II simulations. Atmos. Chem. Phys. 13, 1853–1877. http://dx.doi.org/10.5194/acp-13-1853-2013.
Noh, Y.M., Müller, D., Shin, D.H., Lee, H., Jung, J.S., Lee, K.H., Cribb, M., Li, Z., Kim, Y.J., 2009. Optical and microphysical properties of severe haze and smoke aerosol measured by integrated remote sensing techniques in Gwangju, Korea. Atmos. Environ. 43, 879–888. http://dx.doi.org/10.1016/j.atmosenv.2008.10.058.
Noh, Y.M., Müller, D., Mattis, I., Lee, H., Kim, Y.J., 2011. Vertically resolved light-absorption characteristics and the influence of relative humidity on particle properties: multiwavelength Raman lidar observations of East Asian aerosol types over Korea. J. Geophys. Res. 116, D06206. http://dx.doi.org/10.1029/2010JD014873.
Noh, Y.M., Müller, D., Lee, H., Lee, K., Kim, K., Shin, S., Kim, Y.J., 2012. Estimation of radiative forcing by the dust and non-dust content in mixed East Asian pollution plumes on the basis of depolarization ratios measured with lidar. Atmos. Environ. 61, 221–231. http://dx.doi.org/10.1016/j.atmosenv.2012.07.034.
Noh, Y.M., 2014. Single-scattering albedo profiling of mixed Asian dust plumes with multiwavelength Raman lidar. Atmos. Environ. 95, 305–317.
Ohara, T., Akimoto, H., Kurokawa, J., Horii, N., Yamaji, K., Yan, X., Hayasaka, T., 2007. An Asian emission inventory of anthropogenic emission sources for the period 1980-2020. Atmos. Chem. Phys. 7, 4419–4444.
Papadimas, C.D., Hatzianastassiou, N., Mihalopoulos, N., Kanakidou, M., Katsoulis, B.D., Vardavas, I., 2009. Assessment of the MODIS Collections C005 and C004 aerosol optical depth products over the Mediterranean basin. Atmos. Chem. Phys. 9, 2987–2999. http://dx.doi.org/10.5194/acp-9-2987-2009.
Pappalardo, G., Amodeo, A., Apituley, A., Comeron, A., Freudenthaler, V., Linné, H., Ansmann, A., Bösenberg, J., D'Amico, G., Mattis, I., Mona, L., Wandinger, U., Amiridis, V., Alados-Arboledas, L., Nicolae, D., Wiegner, M., 2014. EARLINET: towards an advanced sustainable European aerosol lidar network. Atmos. Meas. Tech. 7, 2389–2409. http://dx.doi.org/10.5194/amt-7-2389-2014.
Quaas, J., Boucher, O., Bellouin, N., Kinne, S., 2008. Satellite-based estimate of the direct and indirect aerosol climate forcing. J. Geophys. Res. Atmos. 113 http://dx.doi.org/10.1029/2007JD008962. D05204.
Ramanathan, V., Ramana, M.V., Roberts, G., Kim, D., Corrigan, C., Chung, C., Winker, D., 2007. Warming trends in Asia amplified by brown cloud solar absorption. Nature 448, 575–578. http://dx.doi.org/10.1038/nature06019.
Redemann, J., Turco, R.P., Liou, K.N., Hobbs, P.V., Hartley, W.S., Bergstrom, R.W., Browell, E.V., Russell, P.B., 2000. Case studies of the vertical structure of the direct shortwave aerosol radiative forcing during TARFOX. J. Geophys. Res. Atmos. 105, 9971–9979. http://dx.doi.org/10.1029/1999JD901042.
Remer, L.A., Kaufman, Y.J., 2006. Aerosol direct radiative effect at the top of the atmosphere over cloud free ocean derived from four years of MODIS data. Atmos. Chem. Phys. 6, 237–253. http://dx.doi.org/10.5194/acp-6-237-2006.
Remer, L.A., Kleidman, R.G., Levy, R.C., Kaufman, Y.J., Tanré, D., Mattoo, S., Martins, J.V., Ichoku, C., Koren, I., Yu, H., Holben, B.N., 2008. Global aerosol climatology from the MODIS satellite sensors. J. Geophys. Res. 113 http://dx.doi.org/10.1029/2007JD009661.
Ricchiazzi, P., Yang, S., Gautier, C., Sowle, D., 1998. SBDART: a research and teaching software tool for plane-parallel radiative transfer in the Earth's atmosphere. Bull. Am. Meteorol. Soc. 79, 2101–2114. http://dx.doi.org/10.1175/1520-0477(1998)079. <2101:SARATS>2.0.CO;2.
Russell, P.B., Bergstrom, R.W., Shinozuka, Y., Clarke, A.D., DeCarlo, P.F., Jimenez, J.L., Livingston, J.M., Redemann, J., Dubovik, O., Strawa, A., 2010. Absorption Angstrom Exponent in AERONET and related data as an indicator of aerosol composition. Atmos. Chem. Phys. 10, 1155–1169. http://dx.doi.org/10.5194/acp-10-1155-2010.
Samset, B.H., Myhre, G., 2011. Vertical dependence of black carbon, sulphate and biomass burning aerosol radiative forcing. Geophys. Res. Lett. 38 http://dx.doi.org/10.1029/2011GL049697. L24802.
Schulz, M., Textor, C., Kinne, S., Balkanski, Y., Bauer, S., Berntsen, T., Berglen, T., Boucher, O., Dentener, F., Guibert, S., Isaksen, I.S.A., Iversen, T., Koch, D., Kirkevåg, A., Liu, X., Montanaro, V., Myhre, G., Penner, J.E., Pitari, G., Reddy, S., Seland, ø., Stier, P., Takemura, T., 2006. Radiative forcing by aerosols as derived from the AeroCom present-day and pre-industrial simulations. Atmos. Chem. Phys. 6, 5225–5246. http://dx.doi.org/10.5194/acp-6-5225-2006.
Shell, K.M., Somerville, R.C.J., 2007. Direct radiative effect of mineral dust and volcanic aerosols in a simple aerosol climate model. J. Geophys. Res. 112 http://dx.doi.org/10.1029/2006JD007197. D03205.
Shimizu, A., Sugimoto, N., Matsui, I., Arao, K., Uno, I., Murayama, T., Kagawa, N., Aoki, K., Uchiyama, A., Yamazaki, A.A., 2004. Continuous observations of Asian dust and other aerosols by polarization lidars in China and Japan during ACE-Asia. J. Geophys. Res. 109, D19S17. http://dx.doi.org/10.1029/2002JD003253.
Shin, S.K., Müller, D., Lee, C., Lee, K.H., Shin, D.H., Kim, Y.J., Noh, Y.M., 2015. Vertical variation of optical properties of mixed Asian dust/pollution plumes according to pathway of air mass transport over East Asia. Atmos. Chem. Phys. 15, 6707–6720.
Sissenwine, N., Dubin, M., Wexler, H., 1962. The U.S. Standard atmosphere, 1962. J. Geophys. Res. 67, 3627–3630. http://dx.doi.org/10.1029/JZ067i009p03627.
Sugimoto, N., Uno, I., 2009. Observation of Asian Dust and Air-pollution Aerosols Using a Network of Ground-based Lidars (ADNet): Realtime Data Processing for Validation/assimilation of Chemical Transport Models. In: IOP Conference Series: Earth and Environmental Science, 7. http://dx.doi.org/10.1088/1755-1307/7/1/012003, 012003.
Sundström, A.-M., Arola, A., Kolmonen, P., Xue, Y., de Leeuw, G., Kulmala, M., 2015. On the use of a satellite remote-sensing-based approach for determining aerosol direct radiative effect over land: a case study over China. Atmos. Chem. Phys. 15, 505–518. http://dx.doi.org/10.5194/acp-15-505-2015.
Tegen, I., Lacis, A.A., Fung, I., 1996. The influence on climate forcing of mineral aerosols from disturbed soils. Nature 380, 419–422. http://dx.doi.org/10.1038/380419a0.
Tesche, M., Müller, D., Ansmann, A., Hu, M., Zhang, Y., 2008. Retrieval of microphysical properties of aerosol particles from one-wavelength Raman lidar and multiwavelength Sun photometer observations. Atmos. Environ. 42,

6398–6404. http://dx.doi.org/10.1016/j.atmosenv.2008.02.014.
Tesche, M., Ansmann, A., Müller, D., Althausen, D., Engelmann, R., Freudenthaler, V., Groß, S., 2009. Vertically resolved separation of dust and smoke over Cape Verde using multiwavelength Raman and polarization lidars during Saharan Mineral Dust Experiment 2008. J. Geophys. Res. 114, D13202. http://dx.doi.org/10.1029/2009JD011862.
Tesche, M., Müller, D., Gross, S., Ansmann, A., Althausen, D., Freudenthaler, V., Weinzierl, B., Veira, A., Petzold, A., 2011. Optical and microphysical properties of smoke over Cape Verde inferred from multiwavelength lidar measurements. Tellus 63B, 677–694.
Torres, O., Bhartia, P.K., Herman, J.R., Ahmad, Z., Gleason, J., 1998. Derivation of aerosol properties from satellite measurements of backscattered ultraviolet radiation: theoretical basis. J. Geophys. Res. Atmos. 103, 17099–17110. http://dx.doi.org/10.1029/98JD00900.
Veselovskii, I., Kolgotin, A., Griaznov, V., Müller, D., Wandinger, U., Whiteman, D.N., 2002. Inversion with regularization for the retrieval of tropospheric aerosol parameters from multiwavelength lidar sounding. Appl. Opt. 41, 3685. http://dx.doi.org/10.1364/AO.41.003685.
Vuolo, M.R., Schulz, M., Balkanski, Y., Takemura, T., 2014. A new method for evaluating the impact of vertical distribution on aerosol radiative forcing in general circulation models. Atmos. Chem. Phys. 14, 877–897. http://dx.doi.org/10.5194/acp-14-877-2014.
Welton, E.J., Campbell, J.R., Spinhirne, J.D., Scott III, V.S., 2001. Global monitoring of clouds and aerosols using a network of micropulse lidar systems. In: Proc. SPIE 4153, Proc. SPIE 4153, Lidar Remote Sensing for Industry and Environment Monitoring, pp. 151–158. http://dx.doi.org/10.1117/12.417040.
Winker, D.M., Pelon, J.R., McCormick, M.P., 2003. The CALIPSO mission: spaceborne lidar for observation of aerosols and clouds. In: Proc. SPIE 4893, Lidar Remote Sensing for Industry and Environment Monitoring III, 1–11. http://dx.doi.org/10.1117/12.466539.
Winker, D.M., Vaughan, M.A., Omar, A., Hu, Y., Powell, K.A., Liu, Z., Hunt, W.H., Young, S.A., 2009. Overview of the CALIPSO mission and CALIOP data processing algorithms. J. Atmos. Ocean. Technol. 26, 2310–2323. http://dx.doi.org/10.1175/2009JTECHA1281.1.
Winker, D.M., Pelon, J., Coakley, J.A., Ackerman, S.A., Charlson, R.J., Colarco, P.R., Flamant, P., Fu, Q., Hoff, R.M., Kittaka, C., Kubar, T.L., Le Treut, H., McCormick, M.P., Mégie, G., Poole, L., Powell, K., Trepte, C., Vaughan, M.A., Wielicki, B.A., 2010. The CALIPSO mission: a global 3D view of aerosols and clouds. Bull. Am. Meteorol. Soc. 91, 1211–1229. http://dx.doi.org/10.1175/2010BAMS3009.1.
Won, J.-G., Yoon, S.-C., Kim, S.-W., Jefferson, A., Dutton, E.G., Holben, B.N., 2004. Estimation of direct radiative forcing of Asian dust aerosols with sun/sky radiometer and lidar measurements at Gosan, Korea. J. Meteorol. Soc. Jpn. 82, 115–130. http://dx.doi.org/10.2151/jmsj.82.115.
Zarzycki, C.M., Bond, T.C., 2010. How much can the vertical distribution of black carbon affect its global direct radiative forcing? Geophys. Res. Lett. 37, L20807. http://dx.doi.org/10.1029/2010GL044555.